# A Thermal Plume Model for the Convective Boundary Layer: Representation of Cumulus Clouds

CATHERINE RIO AND FRÉDÉRIC HOURDIN

*Laboratoire de Météorologie Dynamique du CNRS, IPSL, Paris, France*

(Manuscript received 21 July 2006, in final form 16 May 2007)

ABSTRACT

The "thermal plume model," a mass-flux scheme combined with a classical diffusive approach, originally developed to represent turbulent transport in the dry convective boundary layer, is extended here to the representation of cloud processes. The modified parameterization is validated in a 1D configuration against results of large eddy simulations (LES), as well as in a 3D configuration against in situ measurements, for a series of cases of dry and cloudy convective boundary layers. Accounting for coherent structures of the mixed layer with the mass-flux scheme improves the representation of the diurnal cycle of the boundary layer, particularly its progressive deepening during the day and the associated near-surface drying. Results also underline the role of the prescription of the mixing of air between the plume and its environment, and of submean-plume fluctuations.

## 1. Introduction

Most diurnal cycles of cloud systems like dispersion of early fog, occurrence of cumuli after a sunny morning, or stormy weather at the end of the day are not well represented in general circulation models (GCMs). It is a concern for climate modeling because of the key role of clouds in the radiative and water budgets. Most GCMs underestimate middle and low clouds from shallow convection (Zhang et al. 2005), while the radiative feedback associated with low-level clouds is a major source of uncertainty for current climate change predictions with GCMs (Bony et al. 2006). The diurnal phasing of deep convection is also a challenge, the peak of deep convection being generally simulated too early in the day (Guichard et al. 2004). A better representation of transport processes in the convective boundary layer (CBL) is probably one of the key issues to improve the representation of those various aspects in GCMs.

In the CBL, turbulence occurs at various scales. Small-scale turbulence dominates in the unstable surface layer, while thermal plumes or cells with an extension comparable to the height of the boundary layer play a key role in the mixed layer. Those coherent structures transport heat upward from the surface layer, even though the upper part of the CBL is generally stably stratified. Velocities of several meters per second encountered here and upgradient turbulent fluxes cannot be represented by a traditional diffusivity model, which assumes that turbulence occurs at smaller scales than that of the vertical variations of mean variables. Deardorff (1972) proposed to solve the problem of the representation of upgradient fluxes by introducing a countergradient term. This approach was refined later by Troen and Mahrt (1986) and Holtslag and Boville (1993). Stull (1984) proposed to cut radically with the diffusive approach by introducing a transilient matrix, which represents exchanges between all the layers of the CBL. A parameterization was derived in this framework by Pleim and Chang (1992) and Alapaty et al. (1997). The mass-flux concept (Arakawa and Schubert 1974; Yanai et al. 1973), in which the atmospheric column is divided into at least two subcolumns of either rising or subsiding air, is also the basis of various parameterizations. For the CBL, this framework has been applied in the past essentially in the form of bulk models in which it is assumed that, in the CBL, the conserved quantities are prescribed a priori, as constants (Betts 1973; Lilly 1968; Randall et al. 1992), or as linear functions of height (Albrecht 1979; Wang and Albrecht

*Corresponding author address:* Catherine Rio, Laboratoire de Météorologie Dynamique, UPMC, Tour 45-55, 3ème étage, BP-99, Jussieu, 4 place Jussieu, 75 005 Paris, France.
E-mail: catherine.rio@lmd.jussieu.fr

DOI: 10.1175/2007JAS2256.1

1990). In those approaches, the closure specification is used to compute an entrainment flux at the top of the CBL. Bulk mass-flux models were generally derived to analyze the physics of the CBL, but some were also used as actual parameterizations for circulation models (Suarez et al. 1983). Mass-flux parameterizations were also developed for the representation of cumulus convection (Tiedtke 1989; Emanuel 1993) but little effort has been made so far to unify boundary layer and cumulus mass-flux schemes.

The scheme developed here attempts to represent the processes in the whole CBL, by considering thermal plumes from the surface to the top of the cloud layer and turbulent eddies in the surface layer. For this, we combine a mass-flux closure with a turbulent diffusive one. Such an approach was first proposed by Chatfield and Brost (1987), whose scheme was never tested in GCMs. On similar ideas, Lappen and Randall (2001a,b,c) proposed to combine the turbulent kinetic energy equation with a mass-flux approach to derive closure relationships for the mass-flux and width of the thermals. Abdella and McFarlane (1997) used a mass-flux approach to parameterize third-order moments in Mellor and Yamada (1974) turbulent equations. On views more similar to Chatfield and Brost (1987), Hourdin et al. (2002, hereafter H02) proposed to make the diffusive scheme of Mellor and Yamada (1974) coexist with a mass-flux parameterization inspired by those developed for deep convection to represent the convective structures observed in the dry boundary layer.

In this parameterization, the existence of a thermal plume originating from the unstable surface layer is considered, the diffusive scheme being still active in the surface layer. A similar parameterization has been developed independently by Siebesma et al. (2007) and tested in a mesoscale model by Soares et al. (2004). Main differences between this latter scheme and the scheme presented in this study concern the geometry of the thermal and the closure relationship. In Soares et al. (2004), the area covered by the plume is vertically constant whereas it is predicted according to entrainment and detrainment in H02. Concerning the closure relationship, the scheme presented in Soares et al. (2004) determines the mass-flux at cloud base as the product of an estimated core fraction and the vertical velocity, whereas H02 use the maximum of convective potential energy inside the plume to compute the mass flux at the top of the unstable layer. Initialization of the updraft is also computed differently. While the properties of the plume within the surface layer are computed using surface fluxes and kinetic energy in Soares et al. (2004), they are computed in H02 from the entrainment of air from the surface layer. The entrainment rate is determined from the buoyancy of air parcels in the (unstable) surface layer. This implies that the vertical discretization should be fine enough to at least crudely represent this surface layer.

The aim of this paper is to extend the so-called thermal plume model of H02 to the representation of shallow cumulus convection, focusing on the diurnal cycle over land. For this, we introduce the condensation processes and associated energy budget inside the plume, and the coupling between the thermal plume model and the statistical cloud scheme of Bony and Emanuel (2001). The first tests performed with the new scheme showed that, without lateral entrainment all along the plume, the additional heating by condensation produces plumes which penetrate too far in the free troposphere. An additional entrainment of environmental air all along the plume is introduced to override this effect. Indeed, tests performed with various assumptions point to the key role of lateral entrainment specification.

Two complementary approaches are used for model evaluation. In the first one, a single-column version of the Laboratoire de Météorologie Dynamique GCM (LMDZ) is evaluated against large eddy simulations (LES) of a series of cases of dry convection (Ayotte et al. 1996), and of a case of cumulus convection over land, the Global Energy and Water Cycle Experiment (GEWEX) Cloud System Study (GCSS) Atmospheric Radiation Measurements (ARM) cumulus case (Brown et al. 2002). An intercomparison of single-column models on that case (Lenderink et al. 2004) underlines the role of the coupling between turbulence and convection. Comparisons with LES allowed us to assess the validity of the physical concepts at the basis of the thermal plume model and to fix model parameters. The robustness of the scheme with regard to those parameters is evaluated by testing it on another shallow convective case, the oceanic case Barbados Oceanographic and Meteorological Experiment (BOMEX; Siebesma et al. 2003). In the second approach, the full 3D GCM is used with a stretched grid around a ground-based atmospheric observatory for cloud and aerosol research located near Paris [Site Instrumental de Recherche en Télédétection Atmosphérique (SIRTA); Haeffelin et al. 2005]. Results are compared with observations of three consecutive days with a well-marked diurnal cycle and afternoon convective cumulus.

The paper is organized as follows. The parameterization of the boundary layer and cloud processes in LMDZ is presented in section 2. Section 3 presents results obtained on the dry cases already tested by H02, focusing on the introduction of lateral entrainment. In

section 4, results obtained in the single-column mode on the GCSS ARM cumulus case are presented. Section 5 is devoted to the validation of the scheme in other conditions (BOMEX case and 3D simulations). Conclusions are drawn in section 6.

## 2. Model description

### a. The thermal plume model

In the thermal plume model (H02; see also Coindreau et al. 2007), as in Chatfield and Brost (1987) and Soares et al. (2004), the parameterization of the convective boundary layer combines a classical diffusive approach with a mass-flux scheme. Each column is divided into a mean ascending thermal plume of mass flux $f = \alpha\rho w_u$ (where $\rho$ is the air density, $\alpha$ the fractional cover of the plume and $w_u$ the vertical velocity), and a compensating subsidence in the environment of mass-flux $-f$. Hence, the vertical turbulent flux of a conserved quantity $\psi$ is written

$$\overline{\rho w'\psi'} = -\rho K_z \frac{\partial \psi}{\partial z} + f(\psi_u - \psi_e). \tag{1}$$

Subscript $u$ stands for the updraft and $e$ for the environment. As in classical mass-flux parameterizations of deep convection, the assumption is made that environmental values equal to large-scale values ($\psi_e = \psi$). Computation of $K_z$ relies on a prognostic equation for the turbulent kinetic energy adopting the level 2.5 Yamada (1983) version of the Mellor and Yamada (1974) scheme.

### b. Mass-flux specification

The vertical variation of mass-flux $f$ is computed by specifying an entrainment rate $e$ inside the plume and a detrainment $d$:

$$\frac{\partial f}{\partial z} = e - d, \tag{2}$$

so that the steady-state equation for conserved quantity $\psi_u$ in the plume is written

$$\frac{\partial f\psi_u}{\partial z} = e\psi - d\psi_u. \tag{3}$$

Note that horizontal momentum is also transported by the plume.

In the present study, the entrainment rate is specified as the sum of two terms: $e(z) = a(z) + \beta d(z)$. The first one, $a(z)$, is the entrainment rate corresponding to the air supplied to the basis of the plume (in the unstable surface layer), and the second one is the lateral entrainment rate along the plume (above the surface layer), which was not accounted for in the original mass-flux scheme, and which, for the sake of simplicity, is related to detrainment rate $d(z)$ by a constant factor $\beta$ (see section 2e).

A thermal plume is initiated as soon as an unstable layer is detected near the surface ($\partial\theta_v/\partial z < 0$, where $\theta_v$ is the virtual potential temperature). The top of the unstable surface layer is thus defined as the height of the higher unstable layer above the surface. A vertical profile of lateral entrainment rate $a(z)$ from the unstable surface layer (which may include several model layers) is then computed. For that, we introduce the mass-flux $\Phi$, which would be obtained at the top of the unstable surface layer if no other entrainment than $a(z)$ nor detrainment was accounted for [$\Phi = \int_0^Z a(z)\,dz$, where $Z$ is any height above the last unstable layer]. The normalized entrainment rate $a^* = a/\Phi$ is specified as

$$a^*(z) = \Gamma\sqrt{z}\,\max\left(-\frac{\partial\theta_v}{\partial z}, 0\right), \tag{4}$$

$\Gamma$ being chosen to satisfy $\int_0^\infty a^*\,dz = 1$.

The value of $\Phi$ is the result of the closure relationship (see below) and $\Phi$ is also used to nondimensionalize other mass fluxes: $f = f^*\Phi$, $e = e^*\Phi$, and $d = d^*\Phi$.

### c. Vertical velocities

In frictionless and steady-state conditions, the vertical momentum equation in the plume reads

$$\frac{\partial f w_u}{\partial z} = -d w_u + \alpha g\rho \frac{\theta_{v_u} - \theta_v}{\theta_v}, \tag{5}$$

where it is assumed that air is supplied to the thermal with a zero vertical velocity ($w_e = 0$).

The plume develops until it reaches its level of zero buoyancy and then overshoots until its kinetic energy vanishes, defining two heights: the height of zero buoyancy ($z_{\text{mix}}$) and the maximum height reached by the overshooting plume ($z_{\max}$). At $z_{\text{mix}}$, where $\theta_{v_u} = \theta_v$, without entrainment processes in the CBL, vertical velocity should be maximum, and its square $w^2_{\max}$ twice the convective available potential energy.

### d. The closure equation

In a 2D configuration (roll, see Fig. 1) the horizontal velocity $v$ at which air is supplied to the basis of the thermal relates to the corresponding lateral entrainment rate through $a(z) = \rho(z)v(z)/L$ where $L$ is the distance separating two cells. The aspect ratio of the cell $r = L/z_{\max}$ is fixed to $r = 2$ for all simulations presented here, a typical value from LES (see Moeng and Sullivan 1994). With the assumption that the maxi-

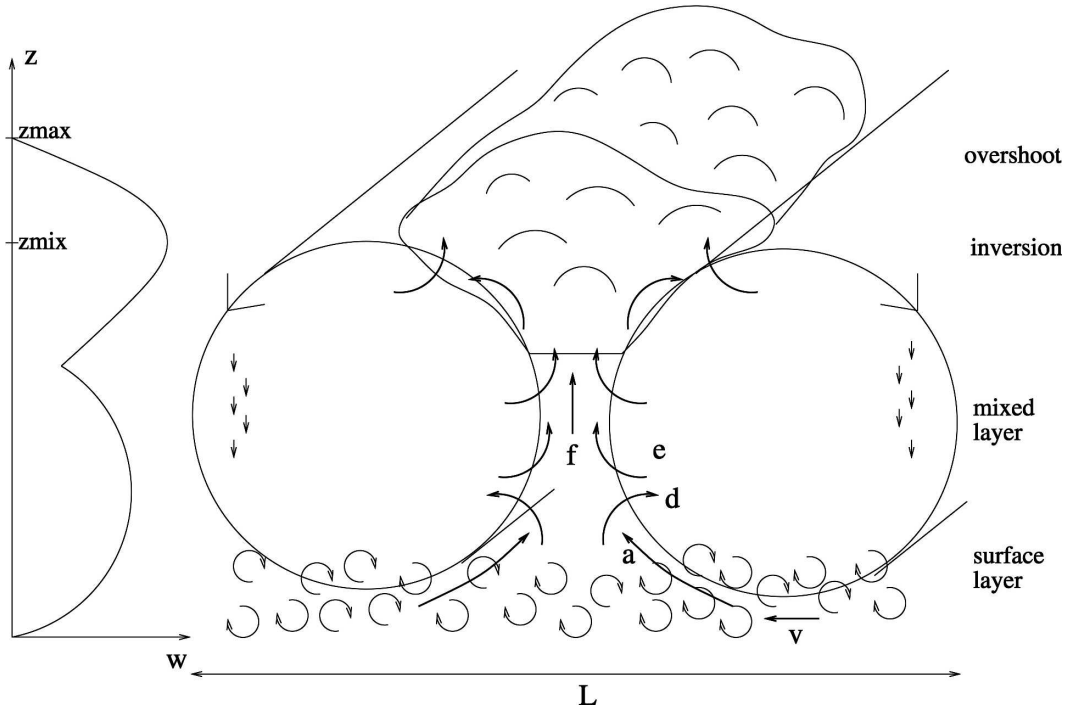


FIG. 1. Physical image sustaining the thermal plume model and corresponding vertical velocity $w$: diffusive turbulence in surface layer and coherent structures in mixed layer. Mass-flux $f$ depends on entrainment of air inside the thermal from the surface layer $a$, above $e$, and detrainment from the plume $d$.

mum vertical velocity in the thermal plume $w_{\max}$ is of the same order of magnitude as the mean horizontal velocity in the unstable surface layer $\upsilon_{\text{moy}}$ (also a result from LES),

$$w_{\max} = \upsilon_{\text{moy}} = \int_{z=0}^{\infty} a^*(z)\upsilon(z)\,dz = \int_{z=0}^{\infty} \frac{a^{*2}(z)\Phi L}{\rho(z)}\,dz, \tag{6}$$

we deduce the closure equation:

$$\Phi = \frac{w_{\max}}{rz_{\max}\displaystyle\int_{z=0}^{\infty} \frac{a^{*2}(z)\,dz}{\rho(z)}}. \tag{7}$$

Physical concepts beyond those choices are discussed in details in H02.

### e. From dry to shallow convection

Latent heat release associated with condensation is accounted for inside the plume. The liquid water potential temperature, defined as the potential temperature of a parcel from which all liquid water would have been evaporated,

$$\theta_l = \theta - \left(\frac{L_\upsilon \theta}{C_p T}\right) r_l, \tag{8}$$

is a conserved quantity both in saturated and unsaturated conditions ($L_\upsilon$ is the latent heat of vaporization, $C_p$ the specific heat at constant pressure, and $r_l$ the liquid water mixing ratio). Characteristics of the thermal are computed by considering as conserved quantities $\theta_l$ and the total water mixing ratio $r_t$.

Lateral entrainment above the surface layer and detrainment are computed as follows. The assumption is made that processes observed in the subcloud layer are the same as those occurring in a dry CBL. Below clouds, we thus keep for detrainment the definition proposed by H02. Below $z_{\text{mix}}$,

$$d(z) = \frac{\partial}{\partial z}\left[\frac{\rho(z)w(z)\sqrt{\lambda z}}{rz_{\max}}\right], \tag{9}$$

where $\lambda$ is a typical length scale. This formulation was deduced from geometrical considerations and expresses the fact that the fraction of the thermal eroded by turbulence increases as $\sqrt{\lambda z}$. Above $z_{\text{mix}}$, and under cloud base, the width of the thermal is reduced following a quadratic decrease so that it should be zero at the top of the CBL in the absence of clouds:

$$d(z) = -\frac{\partial}{\partial z}\left[\rho(z)w(z)\alpha(z_{\mathrm{mix}})\left(\frac{z_{\max}-z}{z_{\max}-z_{\mathrm{mix}}}\right)^2\right]. \tag{10}$$

With those definitions most of the detrainment occurs above $z_{\mathrm{mix}}$ where the stability in the environment increases consistently with commonly admitted ideas (Raymond and Blyth 1986). However LES results suggest that the area covered by the plume stays close to a constant value in the subcloud layer. In this case, the detrainment rate defined in this study between the inversion and cloud base may be too large. Further studies may be conducted with LES to better understand the differences of physical processes occurring in a dry CBL and in a subcloud layer.

A number of reviews (see Blyth 1993), and studies (Siebesma and Cuijpers 1995; Siebesma and Holtslag 1996; Zhao and Austin 2005a,b) using LES, or Zhao and Austin (2003) using episodic mixing and buoyancy-sorting models (EMBS) have been devoted to the evaluation of entrainment and detrainment in clouds. Here, following Tiedtke (1989), we take entrainment and detrainment rates proportional to the mass flux inside the cloud:

$$e^*(z) = \epsilon f^*(z), \tag{11}$$

$$d^*(z) = \delta f^*(z). \tag{12}$$

Siebesma and Cuijpers (1995) showed that entrainment and detrainment rates used in most current parameterizations were one order of magnitude smaller than in LES, and that the detrainment rate was systematically larger than the entrainment rate leading to a mass flux decreasing with height inside the cloud. Siebesma and Holtslag (1996) proposed a range of values for $\epsilon$ and $\delta$ of $\epsilon = 1.5-2.5(\times 10^{-3}\ \mathrm{m}^{-1})$ and $\delta = 2.5-3(\times 10^{-3}\ \mathrm{m}^{-1})$. Those definitions with similar values were also retained by Soares et al. (2004).

To be consistent all along the plume, the entrainment rate in the subcloud layer is taken to be proportional to the detrainment rate with a ratio $\beta = e/d$ fixed like inside the cloud at 0.4. It is considered that, when mixing occurs between the plume and its environment, both entrainment and detrainment processes are enhanced. This assumption may be reconsidered in the future. For instance, Bretherton and Smolarkiewicz (1989) show that entrainment generally occurs where buoyancy increases while it is the opposite for detrainment. Recent studies propose definitions of $\epsilon$ depending on clouds characteristics (Siebesma et al. 2003; Neggers et al. 2002). The parameterization proposed here is kept as simple as possible to make a first step toward improvement of representation of those processes in GCMs. The scheme for entrainment and detrainment finally depends on three parameters: $\lambda$, $\beta$, and $\delta$. Value of parameter $\lambda$ is chosen to have results consistent with LES in both dry and cloudy cases; $\lambda = 30$ m is retained. The value of $\delta$ is then fixed to $\delta = 2.10^{-3}\ \mathrm{m}^{-1}$ using the GCSS ARM cumulus case. The degree of generality of those values is evaluated with the BOMEX oceanic case and 3D simulations.

### f. The cloud scheme

Following Bony and Emanuel (2001), the in-cloud water content $r_{\mathrm{inc}}$ is used as a predictor for cloud fraction $c_f$, together with large-scale total water content $\bar{r}$ and humidity at saturation $r_{\mathrm{sat}}$. Introducing the probability distribution function (PDF) $P(r_t)$ of the subgrid-scale total water with

$$\int_0^\infty P(r)\,dr = 1, \tag{13}$$

the cloud fraction reads

$$c_f = \int_{r_{sat}}^\infty P(r)\,dr, \tag{14}$$

and the in-cloud condensed water is

$$r_{\mathrm{inc}} = \frac{\displaystyle\int_{r_{\mathrm{sat}}}^\infty (r - r_{\mathrm{sat}})P(r)\,dr}{c_f}. \tag{15}$$

For the PDF, we use a generalized lognormal bounded by 0 with a mean $\bar{r}$ and standard deviation $\sigma$. The generalized lognormal distribution has the specificity to include lognormal distributions with both positive and negative skewness. When the ratio $\sigma/\bar{r}$ approaches zero, the distribution tends to a Gaussian. Because the distribution domain is bounded by 0, when $\sigma/\bar{r}$ increases the distribution displays an increasing positive skewness as observed in convective clouds. Here $\sigma$ is estimated in each grid cell, for which the thermal plume model predicts a positive liquid water content, from an inverse procedure, so that the in-cloud water content predicted by the statistical cloud scheme ($r_{\mathrm{inc}}$) equals the condensed water content predicted by the thermal plume scheme ($r_u - r_{\mathrm{sat}}$). The predicted clouds precipitate, and reevaporation in the layers below is also computed (see details in Hourdin et al. 2006). This cloud scheme was evaluated against cloud resolving models (CRMs) for the Tropical Ocean Global Atmosphere Coupled Ocean–Atmosphere Response Experiment (TOGA COARE) but was never tested for shallow convective clouds.

### g. The LMDZ general circulation model

Simulations are run using the most recent version LMDZ4 of the global climate model of the Laboratoire de Météorologie Dynamique (Hourdin et al. 2006), recently involved in the Intergovernmental Panel on Climate Change (IPCC) exercise (Dufresne et al. 2005). Its zooming capability ($Z$ of LMDZ) allows it to focus the horizontal grid on a chosen region. The physical package includes the radiation scheme of Fouquart and Bonnel (1980) for the solar part and of Morcrette et al. (1986) for the infrared part. The deep convection scheme is adapted from Emanuel (1993).

The simulations presented hereafter differ by the boundary layer scheme. In the Mellor and Yamada (MY) simulations, the boundary layer is parameterized using a diffusive approach (Yamada 1983). For the two other simulations, the thermal plume model is used in combination with the same diffusive scheme. In the THdry simulations, the original dry version of the thermal plume model is used. The new version described above is used for the TH simulations. The model is used in both 1D and 3D configurations.

## 3. Dry convective cases

The modified parameterization is first tested in dry conditions, against a series of idealized LESs of water- and cloud-free convection (Ayotte et al. 1996), already used to evaluate the original version of the thermal plume model (H02). For cloud-free cases, the main difference between THdry and TH consists in the lateral entrainment of air into the plume above the surface layer in TH.

### a. The LES cases

The LES code used is fully described by Ayotte et al. (1996). For each case, the grid consists of $96 \times 96 \times 96$ points with various domain sizes, from 1 to 2 km in the vertical and from 2 to 5 km in the horizontal. Simulations MY, THdry, and TH are run with the same vertical resolution as for LES, the time step varying from 15 to 100 s depending on the case. The various cases consider different surface forcing, initial conditions, and geostrophic wind. They are symbolized with a number (corresponding to the value of the surface heat flux), and letters for different initial conditions. For example, simulation 24SC is run with a surface heat flux of 0.24 K m s$^{-1}$ and with a strongly capped (SC) initial potential temperature profile (strong inversion). Cases with a zero surface heat flux are also available, or with an initially weak inversion (WC). As for the geostrophic wind, all simulations labeled WC or SC are constant geostrophic wind cases ($u_g = 15$ m s$^{-1}$ and $v_g = 0$). Simulation 24F has zero geostrophic wind (free convection), and simulations 15B and 24B run with $u_g = 10$ m s$^{-1}$ and $v_g = 0.01 \times z$ m s$^{-1}$.

A passive tracer $B$ is also introduced in the simulations, with $B = 13.5$ below the inversion, $B = 3$ above and a nonzero upward surface flux.

### b. Vertical profiles

Results obtained for simulation 24SC are displayed in Fig. 2 as an example. Figure 2 shows the vertical profiles of wind, potential temperature, and tracer $B$ averaged between times $t_1 = t_0 + 4\tau$ and $t_2 = t_0 + 10\tau$. Here $\tau$ is the large eddy turnover time defined as $\tau = z_i/w_*$, where $z_i$ is the inversion height and $w_*$ the convective velocity scale, which depends on $z_i$, the surface heat flux, and a coefficient of thermal expansion. As already mentioned in H02, THdry improves the results compared with MY, particularly in the representation of the inversion. Results obtained with TH are close to THdry. The upper part of the mixed layer is only slightly warmer with TH and the inversion is not as well captured as with THdry.

### c. Entrainment at the inversion layer

Following Ayotte et al. (1996), we evaluate the various parameterizations comparing, for a scalar $\psi$ ($\theta$ or $B$), the quantity

$$A_1 = \frac{1}{t_f - t_0} \int_{t_0}^{t_f} \overline{w'\psi'}[z_i(t_0), t]\, dt, \tag{16}$$

which represents the averaged flux of $\psi$ through $z_i(t_0)$ between times $t_0$ and $t_f$, that is, the entrainment at the inversion layer. Here $A_1$ is computed from the vertical profiles of $\psi$ at times $t_0$ and $t_f$:

$$A_1 = -\frac{1}{t_f - t_0} \int_{z_i(t_0)}^{H} [\psi(z, t_f) - \psi(z, t_0)]\, dz, \tag{17}$$

where $H$ is any height above CBL top and the final profile of $\psi$ [noted here $\psi(z, t_f)$] the averaged profile between times $t_1$ and $t_2$ [$t_f = (t_1 + t_2)/2$].

The value of this parameter for $\theta$ and $B$ for all various cases is shown in Fig. 3. Simulation MY underestimates the entrainment at the inversion layer for all the convective cases (i.e., except 00SC and 00WC). Results obtained with THdry are more consistent with LES. TH shows a slight overestimation of the transfer across the inversion layer, particularly for the cases with strong surface forcing (24SC and 24F).

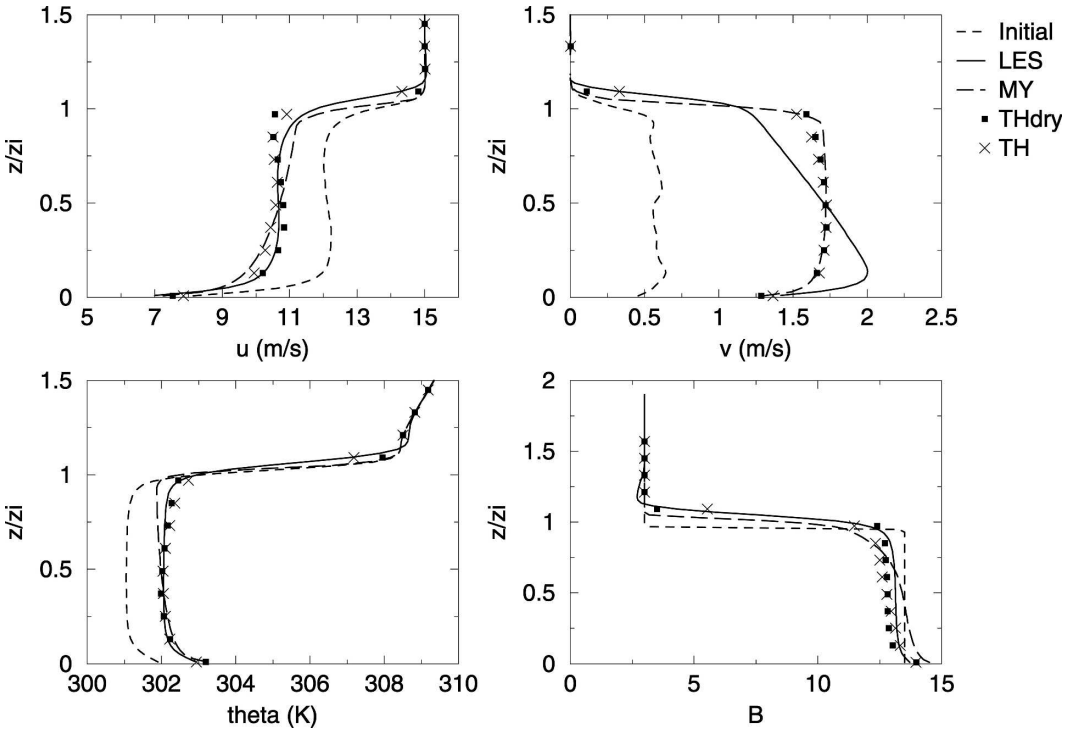


FIG. 2. Dry convective case 24SC: wind speed ($u$ and $v$, m s$^{-1}$), $\theta$ (K) and concentration of tracer $B$ are shown at initial time $t_0$ (dashed line) and averaged between $t_1$ and $t_2$ for the LES and the various parameterizations MY, THdry, and TH.

Sensitivity tests (not shown) indicate that entrainment at the inversion layer is better represented when $\beta$ increases up to 0.6 or 0.8, but the inversion is then too strong. A further increase of $\lambda$ when $\beta = 0.4$ also improves the results. The parameters could be set to improve results in those dry cases, but we conserve $\beta = 0.4$ and $\lambda = 30$, which are also valid for the shallow convective case presented below.

## 4. The GCSS ARM cumulus case

### a. Setup

The present case, built by the GCSS working group, is based on observations made at the ARM Southern Great Plains site in Oklahoma on 21 June 1997 and was also studied within the European Cloud Systems (EUROCS) project. It is a typical case of development

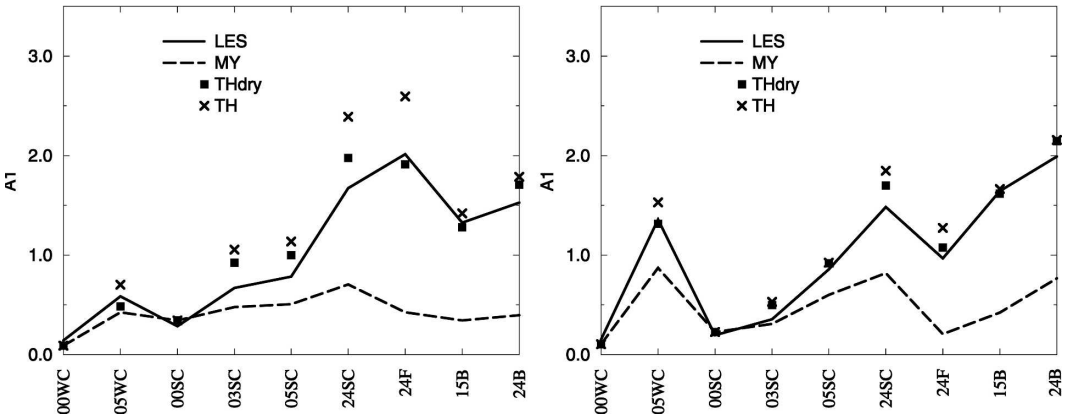


FIG. 3. Coefficient $A_1$ for $\theta$ and $B$ obtained with LES, MY, THdry, and TH and displayed for the various dry convective cases.

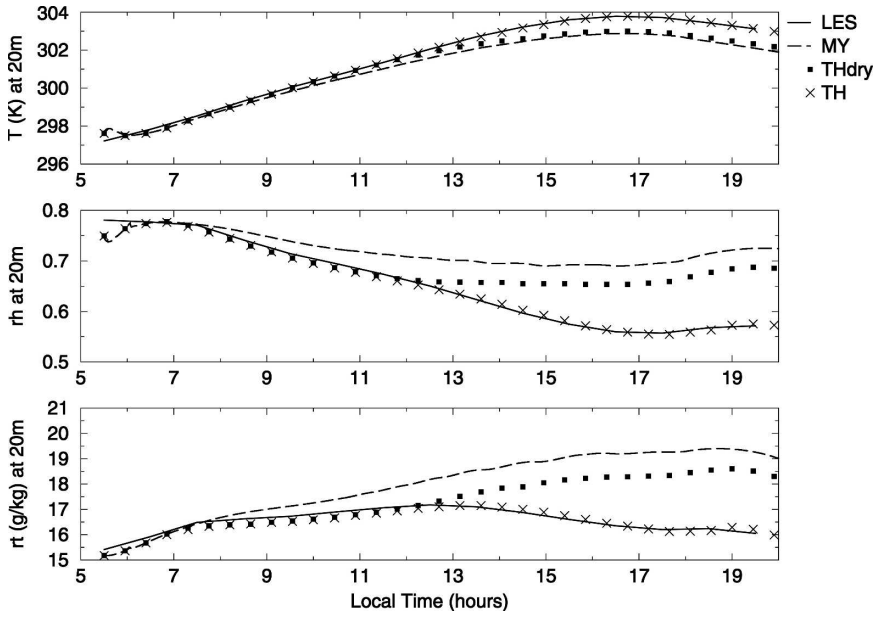


FIG. 4. Temperature ($T$; K), relative humidity (rh), and water mixing ratio (rt; g kg$^{-1}$) at 20 m above surface: comparison of simulations MY, THdry, and TH with LES results for the GCSS ARM cumulus case.

of shallow convection over land. An intercomparison of LES models gave a good agreement with measurements (Brown et al. 2002). In this study we use the results of the Royal Netherlands Meteorological Office (KNMI) LES model also used for an intercomparison study of single-column models (SCMs; Lenderink et al. 2004). It can be seen from that intercomparison that most SCMs overestimate both cloud liquid water and cloud cover associated with unrealistic thermodynamic profiles. The case was developed to study the diurnal cycle of shallow convection over land and surface fluxes evolving during the day with low values at sunrise and sunset and maximal values of 500 W m$^{-2}$ for the latent heat flux and of 140 W m$^{-2}$ for the sensible heat flux around midday. Those surface latent and sensible heat fluxes are prescribed. A simple representation of the large-scale advective tendencies and radiative tendencies is used, their effects being small when compared with those of the surface forcing. Neither the radiation scheme nor the deep convection scheme is activated. The simulations are run with a vertical resolution of 40 layers in the first four kilometers and are running from 0530 to 1945 LT with a 20-s time step.

### b. Large-scale meteorological fields

Figure 4 shows the time evolution of temperature, relative humidity, and water mixing ratio at 20 m above surface (first model layer). When the diffusive scheme is used alone (MY), the first model layer stays too cold and too moist, and relative humidity stays almost constant during the day, while it decreases from 0.8 in the morning to 0.55 in late afternoon in LES. Activation of the thermal plume scheme in the morning (as soon as the surface layer becomes unstable) allows a better mixing in the boundary layer, explaining the faster drying after 0700 LT. The dry and new versions of the thermal plume model (THdry and TH) give results similar with LES until 1200 LT. In early afternoon, when cumulus start to grow, the additional latent heat release in the thermal plume with the TH scheme results in a deeper boundary layer and hence in an additional heating and drying near the surface (due to an enhanced mixing with warm and dry air from the free troposphere), in better agreement with LES. Stevens (2007), using LES and a conceptual model for a CBL developing under the effect of a constant surface buoyancy flux in an atmosphere with constant stratification, also obtains a faster deepening of a cloudy CBL compared with a dry CBL (linearly in time rather than as a square root of time), also associated with a drying near the surface. In Stevens' (2007) conceptual model, the rate at which the cloudy layer deepens is controlled by the evaporative cooling occurring in the inversion layer, resulting from the detrainment of cloud water at the top of cumulus clouds. The evolution of the CBL is illustrated further in Fig. 5, which shows the vertical profiles of potential temperature and total water at various times. At 0930 LT, before cloud formation,

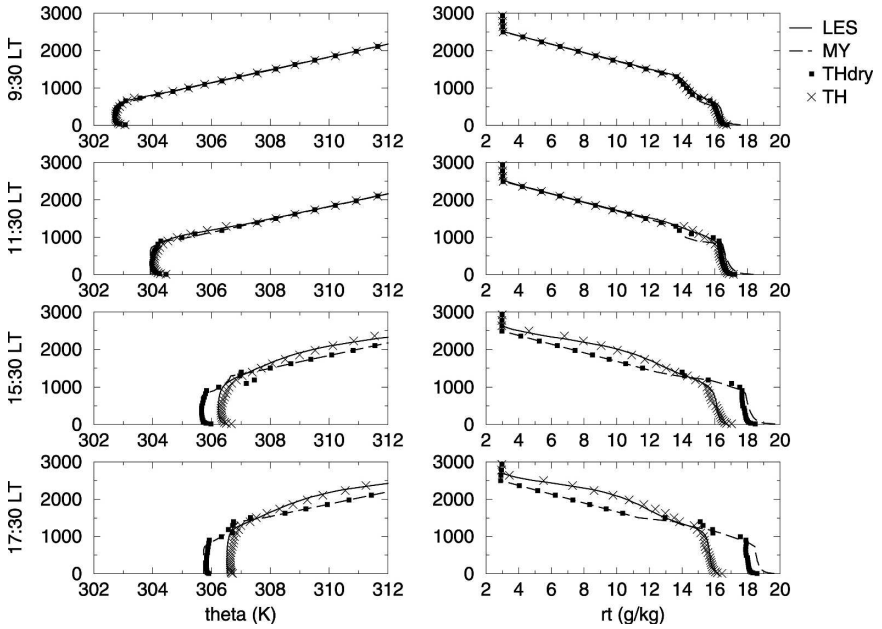


FIG. 5. Vertical profiles of potential temperature ($\theta$) and total water mixing ratio (rt) at 0930, 1130, 1530 and 1730 LT: comparison of simulations MY, THdry, and TH with LES results for the GCSS ARM cumulus case.

THdry and TH give very similar results, and simulation MY is not very different. At 1530 LT the total water obtained with MY and THdry is overestimated below 1000 m and underestimated above, as a consequence of an underestimated vertical transport. Results obtained with TH are more consistent with LES. For MY and THdry, the difference with LES are larger at 1730 LT.

Figure 6 top shows relative humidity and horizontal velocity at 1530 LT. MY and THdry are mutually close, and results obtained with TH are more consistent with LES concerning relative humidity and wind profile, which is better captured than for most simulations presented in Lenderink et al. (2004). Cloud fraction and in-cloud water content are displayed in Fig. 6 bottom for LES and simulation TH. For LES both the "cloud mean" value (average of cells with nonzero liquid water) and the "cloud core" value (cells with liquid water, upward motion, and positive buoyancy) as defined by Siebesma and Cuijpers (1995) are shown. Simulation TH gives in-cloud water content quite consistent with LES core in the lower part of the cloud, but the associated cloud fraction is too low. Between 2500 and 3200 m, LES predicts a very small cloud fraction with large

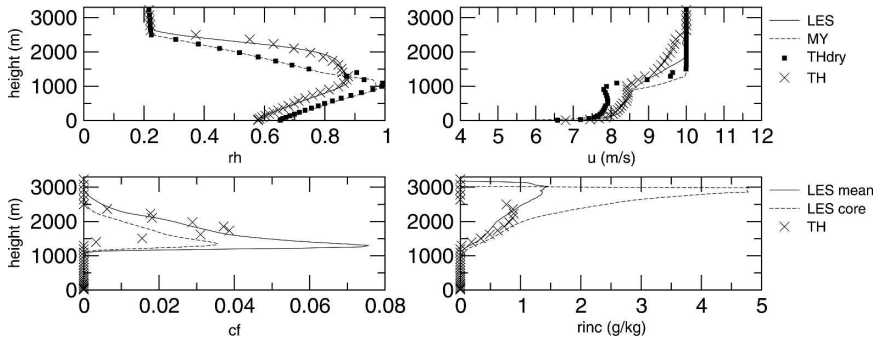


FIG. 6. Vertical profiles of rh and zonal velocity ($u$; m s$^{-1}$) at 1530 LT: comparison of simulations MY, THdry, and TH with LES results for the GCSS ARM cumulus case. Cloud fraction (cf) and in-cloud water content (rinc; g kg$^{-1}$) are also displayed for LES and TH at 1530 LT.

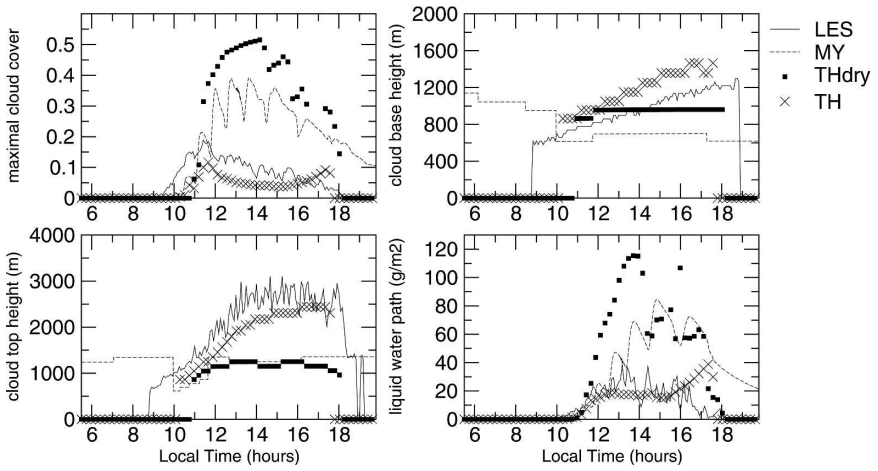


FIG. 7. Time evolution of maximum cloud cover, cloud-base and cloud-top heights, and liquid water path: comparison of simulations MY, THdry, and TH with LES results for the GCSS ARM cumulus case.

in-cloud water while the parameterization does not predict any clouds above 2500 m.

The time evolution of clouds characteristics are shown in Fig. 7. For MY and THdry, the maximal cloud cover (computed as the maximum of cloud fraction over the vertical at each time step), is overestimated and clouds do not vanish at the end of day with MY. With the new version of the thermal plume model (TH), the value obtained is closer to LES but still too low, and the peak at the end of the afternoon should not exist. The onset of cumulus is too late by one hour, and the disaggregation of clouds occurs a little too early. This problem will be discussed in the last part of this section. The new version better represents the increase of the cloud-base height during the day even if its altitude stays too high by 100 m all day. The computation of the cloud-top height is also improved with the new version of the scheme although this value stays a few hundred meters too low. As for liquid water path, results are consistent with cloud cover, with too-low values during the day for TH and an increase at about 1700 LT.

### c. *Inside clouds*

Figure 8 displays the vertical profiles of the entrainment rate in the surface layer and above ($e$), and of the detrainment rate ($d$) at 1530 LT. The detrainment rate increases with height between the inversion and cloud base. In the unstable surface layer, entrainment is maximal in the first layer of the model. Comparison with LES of the total mass flux inside the cloud at 1530 LT is also given in Fig. 8. The mass flux fits the LES at the inversion but then decreases too fast with height. Figure 9 shows the vertical velocity inside the plume at 1530 LT. The updraft is negatively buoyant in the overshooting region just below cloud top. Results are then expected to be close to the core value in the lower part of the cloud and close to the cloud value in the upper part. The thermal plume velocity is in fact close to the core value in the lower half of the cloud but decelerates too fast compared with LES in the upper part. This may suggest that the entrainment rate is too large inside the cloud, inhibiting buoyancy. We also notice that the local minimum of the vertical velocity is located too high.

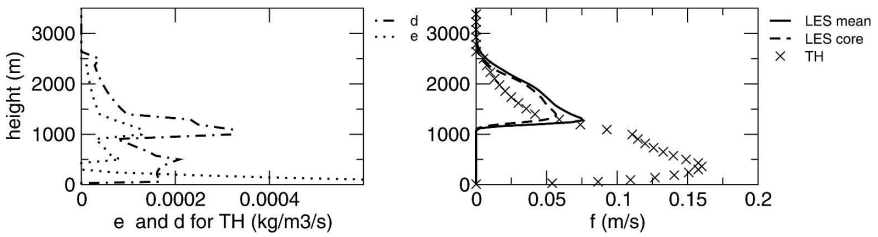


FIG. 8. Vertical profiles of $e$ (from the surface layer and above) and of $d$ at 1530 LT and comparison with LES of $f$ for simulation TH of the GCSS ARM cumulus case.

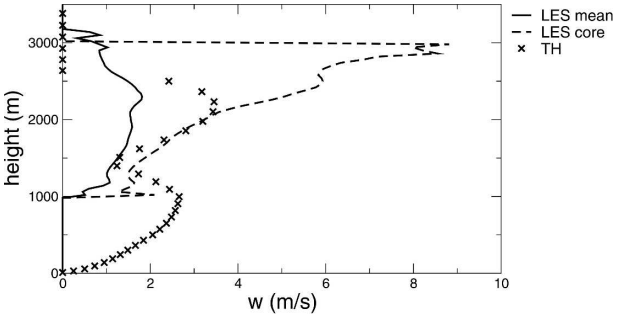


FIG. 9. Vertical profile of $w$ at 1530 LT for simulation TH: comparison with "cloud mean" and "cloud core" values as given by LES (LES data are not available in the subcloud layer).

This joins the fact that the cloud base remains too high during the day. However the shape of the profiles seems to paste to LES, vertical velocity decreases at the base of clouds and then increases until reaching the top.

### d. Higher-order moments

Second- and third-order moments of the vertical wind are compared with LES in Fig. 10. For the thermal plume, those moments are computed as follows:

$$\overline{\psi'^2} = \frac{\alpha}{1-\alpha}(\psi_u - \psi)^2, \tag{18}$$

$$\overline{\psi'^3} = \frac{\alpha(1-2\alpha)}{(1-\alpha)^2}(\psi_u - \psi)^3. \tag{19}$$

The second-order moments for the vertical wind given by LES include both explicit large eddies (resolved scale) and parameterized subgrid scales, while TH results concern the contribution of the thermals only. As already discussed by H02, the turbulent fluctuations of $w$ associated with symmetric small-scale turbulence, not accounted for by the mass-flux scheme, explain the strong underestimation of $w'^2$ when compared with LES results. On the other hand those fluctuations have a relatively low contribution to turbulent fluxes dominated by convective structures. The degree of symmetry of the distribution around the mean value of $w$ can be estimated by considering the third-order moment of $w$. Turbulent diffusion does not contribute to third-order moments, which explains why the results obtained with the thermal plume model are in better agreement with LES. For the same reasons as for $w'^2$, $q'^2$ is also strongly underestimated (results not shown).

### e. Sensitivity to model parameters

The results are quite sensitive to the parameters that control detrainment and entrainment rates. Because of the way detrainment and entrainment are prescribed in our parameterization, parameter $\delta$ controls simultaneously detrainment and entrainment, but in the cloud only. At the opposite, a change of $\beta$ (for a given value of $\delta$) will affect entrainment only, but both below and within the clouds. Of course, both entrainment and detrainment can also be modified indirectly when changing any parameter through modification of mass flux $f$. Figs. 11 and 12 show cloud characteristics and near-surface relative humidity obtained for different values of $\beta$ and $\delta$. A decrease of $\beta$, by reducing the rate of entrained air from the mixed layer in the plume, leads to a moister and more buoyant plume, increasing the

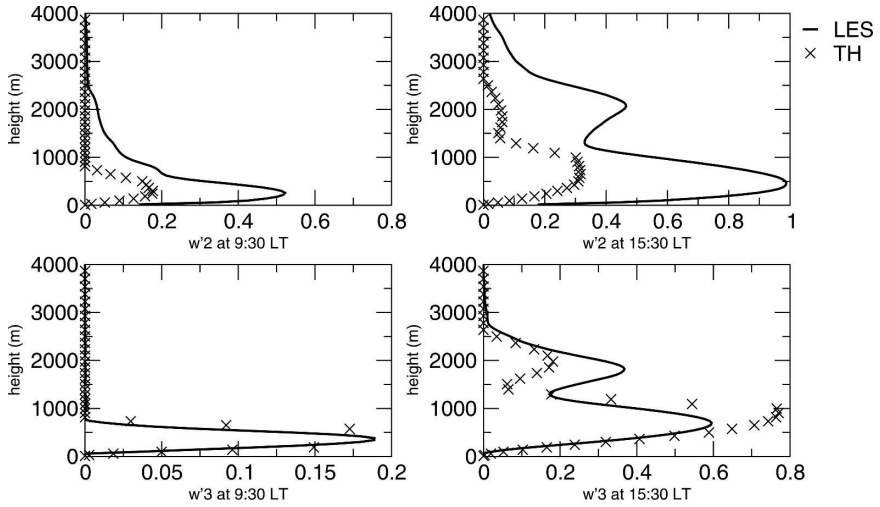


FIG. 10. Comparison with LES of the (top) second- ($m^2\,s^{-2}$) and (bottom) third- ($m^3\,s^{-3}$) order moments of the vertical velocity in the thermal plume at (left) 0930 and (right) 1530 LT for simulation TH of the GCSS ARM cumulus case.

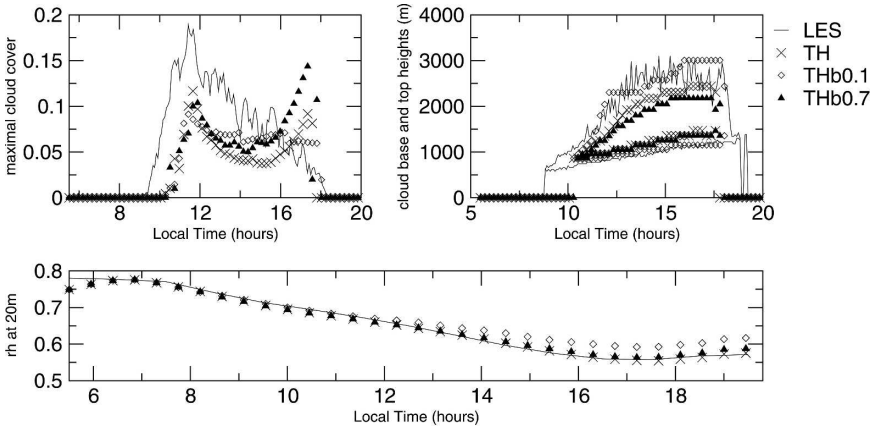


FIG. 11. Sensitivity of cloud characteristics (cloud cover, cloud-base height, and cloud-top height) and near-surface rh to model parameter $\beta$. TH, THb0.1, and THb0.7 correspond to $\beta = 0.4$ (nominal value), $\beta = 0.1$, and $\beta = 0.7$, respectively.

vertical extension of clouds. Indeed, because the plume is moister, it condenses lower, and because it is more buoyant, it overshoots higher. At the same time, as less air is entrained in the plume, the mass flux is smaller, reducing the drying of surface by the compensating subsidence. Parameter $\delta$ has an impact on cloud-top height, illustrating the control of vertical extension of clouds by the environment (Grandpeix et al. 2004). Variation of detrainment—and thus entrainment—rates inside clouds seems to have low feedback on subcloud layer processes (Fig. 12, bottom), at least for the values of $\delta$ tested here. Increasing $\delta$ also strengthens the increase of cloud cover observed around 1730 LT. Indeed, a too-large detrainment rate, by leading to a too-large total water content in the environment associated with a too-small liquid water potential temperature (and thus humidity at saturation), may explain the too-large cloud fraction given by the scheme at that time.

Parameters controlling entrainment and detrainment rates were chosen rather arbitrarily. For example, to reduce the number of those parameters to a minimum, we chose a single value of $\beta$ inside and below the cloud. With this choice it is not possible to change the entrainment rate inside the clouds without changing also entrainment and detrainment rates in the subcloud layer. Taking $\beta$ and $\delta$ as constants over the vertical and in time is another limitation of the scheme: entrainment and detrainment rates may depend on clouds and environmental characteristics, and on turbulence intensity. A lot of studies are focusing on this issue, but physical basements that sustain them are still often contradictory and further work is needed before testing more complex formulations in a GCM parameterization. Here the most suitable parameters to represent mean profiles of humidity and temperature are not the most suitable to represent clouds characteristics. As ra-

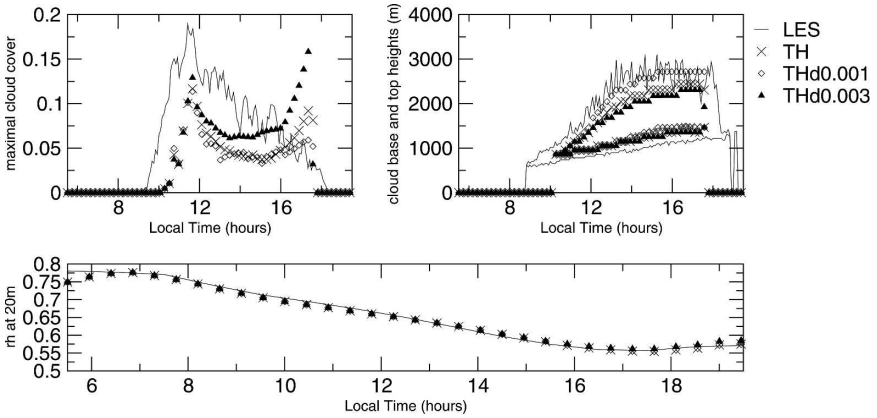


FIG. 12. Sensitivity of cloud characteristics (cloud cover, cloud-base height, and cloud-top height) and near-surface rh to model parameter $\delta$. TH, THd0.001, and THd0.003 correspond to $\delta = 0.002$ (nominal value), $\delta = 0.001$, and $\delta = 0.003$, respectively.

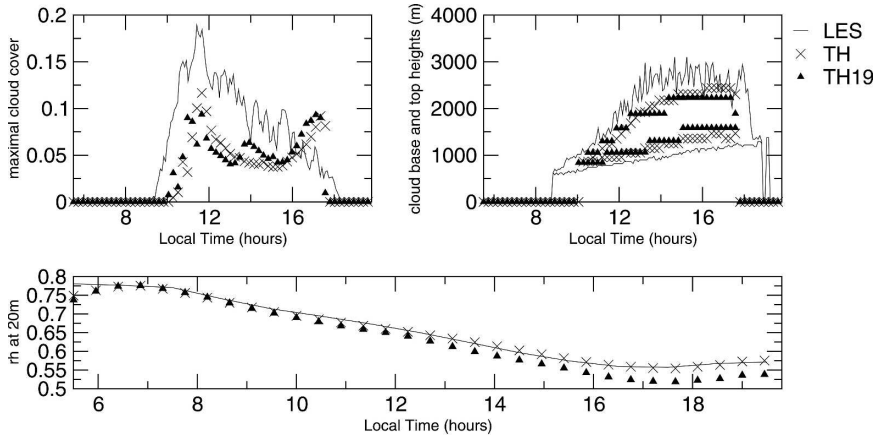


FIG. 13. Sensitivity of cloud characteristics (cloud cover, cloud-base height, and cloud-top height) and near-surface rh to vertical resolution for simulation TH.

diative tendencies are prescribed in that case we chose to keep the parameters that allow an optimal representation of the thermodynamic profiles, taking advantage of the cloud scheme for further improvements.

### f. Sensitivity to vertical resolution

A sensitivity experiment is performed with a 19-layer vertical resolution for the TH case. The thickness of the layers varies progressively from 20 m near the surface to 200 m around 4 km in the 40-layer simulation (with 16 layers below 1000 m); and from 23 to 600 m in the 19-layer simulation (with 10 layers below 1000 m). For the 19-layer case, the model first layer gets too dry during the day (Fig. 13 bottom). Cloud characteristics (Fig. 13 top) do not vary significantly with resolution. In fact, the impact of vertical resolution is small on plume properties but significant on mean profiles. This is explained by the scheme used for discretization of the transport equation. Downward transport in the subsiding environment increases because of a stronger numerical diffusion when a coarser grid is used. This could be solved in the future by replacing the first-order upstream scheme by a less diffusive one.

### g. Adjustment of the cloud scheme

The delay in the clouds onset could be explained by the fact that only a mean thermal is considered where several inhomogeneous thermals may exist in reality. The first clouds probably appear at the top of particularly active and humid thermals. Up to now, the variance $\sigma^2$ of the total water PDF was computed so as to recover the in-cloud water predicted by the mean thermal plume model. To account for thermals variability, an additional variance $\sigma^{*2}$ can be added to $\sigma^2$ for the computation of cloud properties (both cloud fraction and in-cloud liquid water). A test is performed by using a constant value of 0.05 for the ratio $\sigma^*/\bar{r}$. This value is estimated from the difference between TH and LES for the variance of total water. With this modification, the first clouds appear earlier (by about one hour) in better agreement with LES (Fig. 14). The cloud cover is also generally larger and the base lower (both features are

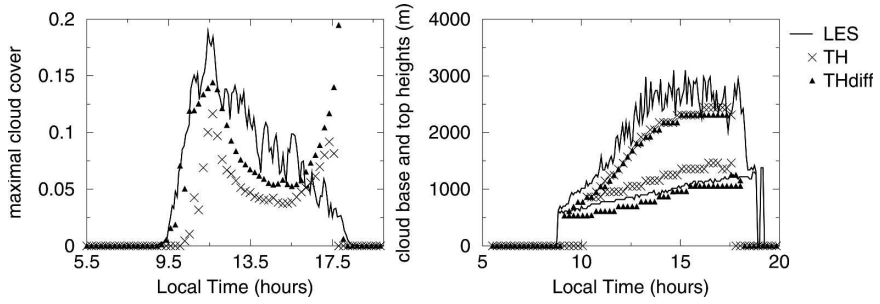


FIG. 14. Influence of submean-plume variability on the cloud scheme for simulation TH: simulation THdiff is run using $\sigma^2 + \sigma^{*2}$ to specify the width of the PDF used in the cloud scheme.

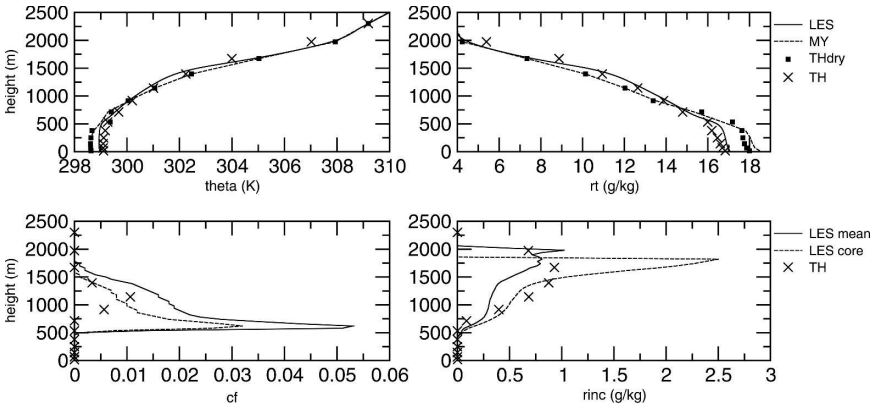


FIG. 15. Vertical profiles of $\theta$ and vapor mixing ratio: comparison of simulations MY, THdry, and TH with LES results for the BOMEX case. Vertical profiles of $f$ and rinc: comparison of simulation TH with LES results for the BOMEX case.

thus improved) while the cloud-top height is almost unchanged. As radiative tendencies are prescribed, the evolution and vertical profiles of temperature, water mixing ratio and relative humidity are almost unchanged with this adjustment (not shown). However the increase of cloud cover in late afternoon is even more pronounced. This may be due to a less active small-scale turbulence at that time than the one represented by the constant value chosen for $\sigma^*/\bar{r}$. Further developments are foreseen to base the computation of $\sigma^*$ on an estimation of the variance of total water due to small-scale turbulence. Nevertheless, given the improvements obtained, simulations in the last part of this study are performed with the present adjustment. However some problems remain in the vertical profile of cloud fraction, with a maximum value not located at cloud base but at the ⅔ of the cloud, and too-low values. This could be explained by the fact that the cloud scheme may present some limitations to represent boundary layer clouds. For example even if the PDF used is a generalized lognormal, the variance of total water is much smaller than the total water in the cell, so that the PDF is close to a Gaussian, making the scheme unable to represent the positive skewness of the distribution of total water content in boundary layer clouds.

## 5. Additional validations

As explained above, the model parameters have been tuned to well reproduce the Ayotte et al. (1996) and the GCSS ARM cumulus cases. It is thus important to check how the scheme behaves under different conditions. For that, we present two cases. One is performed with the same 1D version of the GCM on a case of oceanic cumulus with no diurnal cycle (the BOMEX case), and the second one corresponds to a different case of continental diurnal cycle simulated with the full 3D GCM and compared with in situ observations.

### a. The oceanic case BOMEX

BOMEX is a quasi-steady-state case of trade wind cumulus, built from observations made during an undisturbed period of the Barbados Oceanographic and Meteorological Experiment (Siebesma et al. 2003). Initializations are made using observations averaged over 2 days.

Simulations run over 6 h with a time step of 300 s and a vertical resolution of 19 layers in the first 3 km. Figure 15 (top) displays comparison with LES of averaged values of potential temperature (K) and vapor mixing ratio (g $kg^{-1}$) for simulations MY, THdry, and TH. Figure 15 (bottom) compares LES "cloud mean" and "cloud core" values of cloud fraction and in-cloud water content (g $kg^{-1}$) with TH results. Similar conclusions as for the GCSS ARM cumulus case can be drawn: the thermal plume model adapted for shallow convection (TH) improves the thermodynamic profiles by drying and heating the lower part of the boundary layer and moistening and cooling the upper part compared with other schemes. However the lower part of the CBL is somewhat too dry and hot compared with LES. Again, cloud fraction is too low compared with LES, particularly at cloud base, where maximum of cloud cover is not obtained with TH, while the in-cloud water content is consistent with LES.

### b. Validation in a 3D configuration

SIRTA is a ground-based atmospheric observatory for cloud and aerosol research located near Paris (48°N, 2°E). Remote sensing instruments such as lidars, ra-

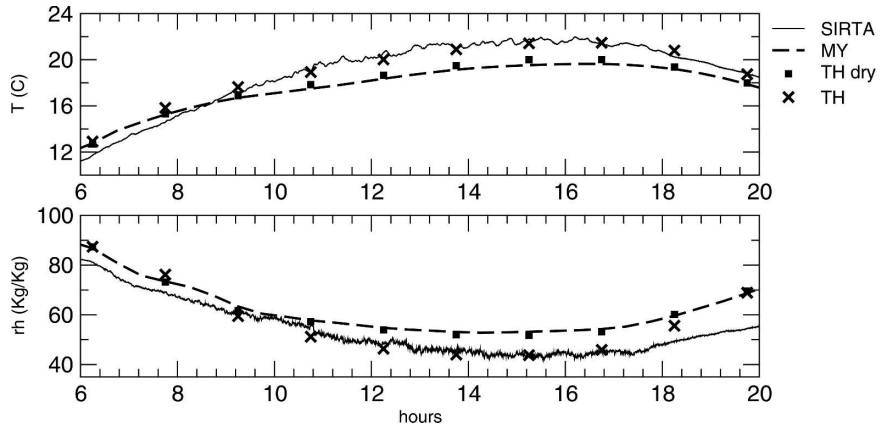


FIG. 16. Comparison of $T$ and rh between the SIRTA observations (at 17 m) and results of simulations MY, THdry, and TH (first layer) averaged over 26, 27, and 28 May 2003.

dars, and radiometers routinely observe atmospheric boundary layer processes like cloud formation, precipitation, or microphysics (Haeffelin et al. 2005). The dry version of the thermal plume model has already been evaluated during the 1-month Water Vapour Profiling Inter-Comparison (VAPIC) campaign (Coindreau et al. 2007), but this period is not well adapted for the study of shallow convection. Here we retain three days in May 2003 corresponding to typical summer conditions with the development of small cumuli after a sunny morning.

The 3D simulations are performed with a global stretched grid of 48 points in longitude and 32 in latitude. The horizontal resolution reaches 120 km near Paris, where SIRTA is located. The time steps for the 3D dynamics and for the parameterized physics are of one and three minutes, respectively, and simulations are run with a vertical resolution of 40 layers for the entire atmosphere, which corresponds to about 15 layers in the first 2 km.

Following Coindreau et al. (2007), temperature, relative humidity, and wind are relaxed toward analysis fields from European Centre for Medium-Range Weather Forecasts (ECMWF) with a time constant of 30 min outside the zoom and 10 days inside (nudging). Smaller time constants are used for the relative humidity (5 h outside and 3 h inside). Thermal conduction in the ground is computed with an 11-layer model. The thermal inertia of the soil is set to 2000 USI. The evaporation is computed as $E = bE_{\text{pot}}$ where the potential evaporation $E_{\text{pot}}$ is that of a free surface of water in the same conditions and $b$ is a parameter fixed to 0.0133, so as to fit the mean trend of mean surface humidity observed during that period. Simulations are run with the standard version of LMDZ from 1 to 19 May 2003. Simulations are then restarted on 20 May 2003 for the different versions. We consider 26, 27, and 28 May 2003 for comparison with SIRTA observations.

Figure 16 shows the diurnal evolution of temperature and relative humidity averaged over the three days studied at 17 m for SIRTA observations and in the first model layer for simulations. Use of the TH scheme significantly improves the representation of the faster heating and drying of the first layer from 0900 LT when cumulus start to develop, as already seen in the GCSS ARM case. On the other hand, at night, neither THdry nor TH affects much the characteristics of the boundary layer. THdry predicts a cloud base close to that derived from lidar measurements (Fig. 17), but the cloud-top height remains too low. TH improves the representation of the cloud-top height while the cloud base is too high. In both cases, results are improved in comparison with MY. Figure 17 also shows the cloud radiative forcing (CRF, total minus clear-sky radiative flux at surface). The clear-sky shortwave radiation is not available from the observations, so the clear-sky radiative forcing computed by the model is also used to determine the observed radiative forcing. The radiative forcing for MY and THdry is too high, and too low but closer to observations for TH.

## 6. Conclusions

The dry thermal plume model of H02 has been extended to the representation of cumulus clouds. Both small-scale turbulent flow in the surface layer and organized flow structures in the mixed layer are accounted for combining a diffusive approach and a mass-flux parameterization. After a series of validation tests summarized in this article, following conclusions can be drawn:

1) As that of Soares et al. (2004), this study confirms the importance of accounting for coherent struc-

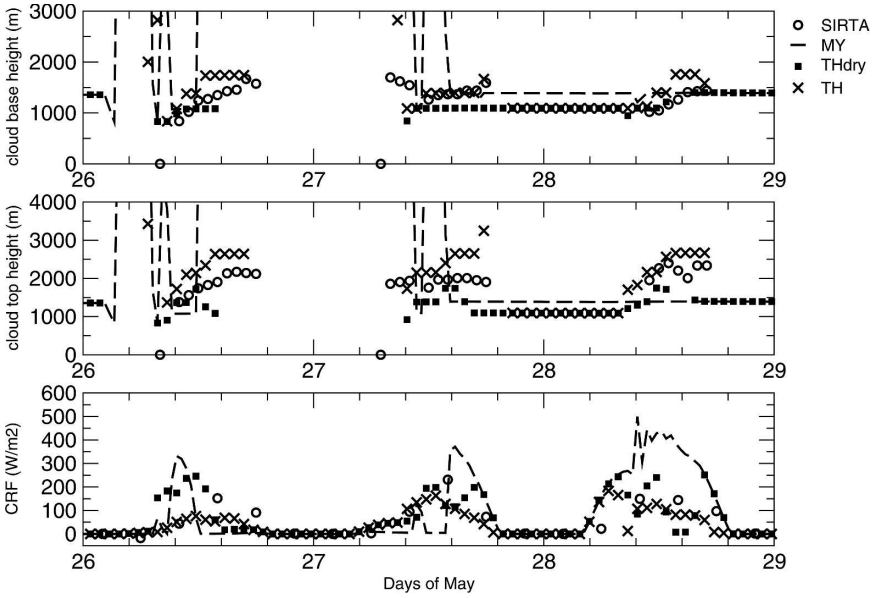


FIG. 17. Cloud-base and cloud-top heights and cloud radiative forcing (CRF; W $m^{-2}$) on 26, 27, and 28 May 2003: comparison of simulations MY, THdry, and TH with combined lidar–radar observations made at SIRTA.

tures for simulation of the diurnal cycle of clear-sky and cumulus-topped convective boundary layer.

2) The series of idealized tests proposed by Ayotte et al. (1996) in various conditions of surface fluxes, vertical temperature profiles, and wind stresses provides a good benchmark for testing boundary layer parameterizations. The improvements observed on those cases when the thermal plume model was added to the Mellor and Yamada diffusive scheme is confirmed here when looking at the diurnal cycle. In particular, the drying of the surface layer associated with the deepening of the boundary layer in the morning is better captured in the GCSS ARM case.
3) Accounting for additional latent heat in the clouds deepens the boundary layer, resulting in a drier near-surface atmosphere in the afternoon, in better agreement with observations [both for the GCSS ARM (Fig. 4) and SIRTA (Fig. 16) cases].
4) The thermal plume model, which specifically accounts for the large-scale part of turbulent transport in the mixed layer (hence strongly underestimating variances), predicts well third-order moments of the distribution of $w'$. This quantity may be used for coupling with deep convection modeling.
5) The thermal plume model also improves the representation of boundary layer wind profiles.

In parallel to those improvements, this study has also identified a number of areas where further research could improve the physical basis of our model. One of them concerns the prescription of entrainment and detrainment rates. As in many other parameterizations, they are prescribed rather arbitrarily. Here we follow Tiedtke (1989), Siebesma and Holtslag (1996), and Soares et al. (2004) to define the entrainment and detrainment rates inside the clouds and results are improved both for the cloud cover and cloud radiative forcing, a very important quantity in the frame of climate applications and climate change simulations. Influence of small-scale turbulence on total water variability in the CBL is also an important issue. The thermal plume model is based on an idealization of a single mean thermal plume, and accounting for "submean-plume" variability may help to predict the time evolution of cloud cover and vertical extension. As a first step, accounting for an additional variance in the prediction of the total water PDF, used to predict clouds, makes the clouds appear earlier (one hour for the GCSS ARM case), in better agreement with observations. This additional variance may of course depend on other conditions, being larger for instance in the very active phase of the growing morning convective boundary layer than in late afternoon. This submean-plume variance could be estimated from the turbulent kinetic energy computed by the MY scheme by adding its vertical transport through the thermal updraft. Also, the turbulent energy would possibly in turn be used to predict entrainment and detrainment. Finally further development of the Bony and Emanuel (2001) cloud

scheme may be conducted to evaluate its ability of representing shallow clouds.

Notwithstanding some previously listed shortcomings, we find that taking into account thermal plumes associated with shallow cumulus significantly improves the representation of the boundary layer in convective conditions.

The next step is to focus on the diurnal cycle of deep convection in LMDZ. As in many other GCMs, deep convection is in phase with solar activity, starting about two hours too early and vanishing at sunset, instead of being maintained during the night. First tests suggest that the thermal plume model, which better represents in the morning the progressive deepening and moistening of the top of the boundary layer, might postpone the onset of deep convection when coupling with the Emanuel (1991) scheme.

*Acknowledgments.* The 1D simulations are performed using the environment of the ARPEGE model and the physics of LMDZ in a single-column mode, ARPEGE being the global climate model developed at CNRM. The authors thus want to thank Pascal Marquet and Marie-Pierre Lefèbvre from CNRM for providing the ARPEGE environment, and the GCSS ARM cumulus and BOMEX cases. They are also very grateful to K. W. Ayotte and G. Lenderink and A. P. Siebesma for the availability of the large eddy simulations used in this study. We would also like to thank Martial Haeffelin and the SIRTA team for providing the data shown in this paper, and Jean-Yves Grandpeix, Anne Mathieu, and Alain Lahellec for their contribution to this work through profitable discussions. The authors also thank Bjorn Stevens and two anonymous reviewers for their constructive comments, which helped to improve the original manuscript.

## APPENDIX

### The Discrete Formulation of the New Thermal Plume Model

The different steps presented in Coindreau et al. (2007) are unchanged, but the equations are modified to take into account the condensation process and the effects of entrainment and detrainment along the plume.

1) Computation of discrete entrainment and detrainment rates integrated over the thickness $\Delta z_k$($E_k^* = e_k^* \Delta z_k$, $A_k^* = a_k^* \Delta z_k$, $D_k^* = d_k^* \Delta z_k$) of layer $k$:

$$A_k^* = c\sqrt{z}_k \Delta\theta_k, \tag{A1}$$

where $c$ is chosen to have $\Sigma\, A_k^* = 1$,

$$D_k^* = \frac{1}{r z_{t_0} \Phi_0}\left(\rho_{k+1/2} w_{k+1/2}\sqrt{\lambda z_{k+1/2}} - \rho_{k-1/2} w_{k-1/2}\sqrt{\lambda z_{k-1/2}}\right) \tag{A2}$$

below cloud base, and

$$D_k^* = \delta f_k^* \Delta z_k \tag{A3}$$

inside the cloud. Here $z_{t_0}$ and $\Phi_0$ are respectively the thermal plume height and the variable $\Phi$ computed at the previous time step.

Entrainment is then computed as

$$E_k^* = \beta D_k^* + A_k^*. \tag{A4}$$

2) Determination of virtual potential temperature $\hat{\theta}_{vk}$ and vertical velocity $w_k$ inside the plume at each level. Liquid water potential temperature and total water mixing ratio at each level are first computed:

$$\hat{\theta}_l = \frac{\sum_{k=1}^{k=l} E_k^* \theta_k}{F_{l+1/2}^* + D_l^*} \tag{A5}$$

and

$$r_{t_l} = \frac{\sum_{k=1}^{k=l} E_k^* r_{t_k}}{F_{l+1/2}^* + D_l^*} \tag{A6}$$

with

$$F_{l+1/2}^* = \sum_{k=1}^{k=l} (E_k^* - D_k^*). \tag{A7}$$

The liquid water mixing ratio is determined by $r_{l_k} = \max(r_{t_k} - r_{\mathrm{sat}_k}, 0)$, where an iterative procedure on temperature is used to solve the Clausius–Clapeyron equation to take into account the variation of $r_{\mathrm{sat}}$ with temperature.

The virtual potential temperature is computed as

$$\hat{\theta}_{v_k} = \hat{\theta}_k(1 + 0.61 r_k - r_{l_k}). \tag{A8}$$

The equation determining the vertical velocity is modified by introducing the effect of detrainment of air in layer $k$:

$$\frac{1}{2} w_{l+1/2}^2 = \frac{1}{2}\left(\frac{F_{l-1/2}^* - D_l^*}{F_{l+1/2}^*} w_{l-1/2}\right)^2 + g\,\frac{\hat{\theta}_l - \theta_l}{\theta_l}(z_{l+1/2} - z_{l-1/2}). \tag{A9}$$

3) As for the closure relation, only the entrainment from the unstable layers must be considered—as in Coindreau et al. (2007)—and

$$\Phi = \frac{w_{\max}}{rz_{\max}\sum_{k=1}^{\text{lentr}} \frac{A_k^{*2}}{\rho_k \Delta z_k}} \tag{A10}$$

with

$$w_{\max} = \sum_{k=1}^{\text{lentr}} A_k^* \upsilon_k. \tag{A11}$$

4) Computation of the entrainment and detrainment rates, $A_k = \Phi A_k^*$, $E_k = \Phi E_k^*$, $D_k = \Phi D_k^*$, and of the final mass flux, $F_{k+1/2} = \Phi F_{k+1/2}^*$.

## REFERENCES


Abdella, K., and N. McFarlane, 1997: A new second-order turbulence closure scheme for the planetary boundary layers. *J. Atmos. Sci.,* **54,** 1850–1867.

Alapaty, K., J. E. Pleim, S. Raman, D. S. Niyogi, and D. W. Byun, 1997: Simulation of atmospheric boundary layer processes using local- and nonlocal-closure schemes. *J. Appl. Meteor.,* **36,** 214–233.

Albrecht, B. A., 1979: A model of the thermodynamic structure of the trade-wind boundary layer: Part II. Applications. *J. Atmos. Sci.,* **36,** 90–98.

Arakawa, A., and W. H. Schubert, 1974: Interaction of a cumulus cloud ensemble with the large-scale environment. Part I. *J. Atmos. Sci.,* **31,** 674–701.

Ayotte, K. W., and Coauthors, 1996: An evaluation of neutral and convective planetary boundary-layer parameterizations relative to large eddy simulations. *Bound.-Layer Meteor.,* **79,** 131–175.

Betts, A., 1973: Non-precipitating convection and its parameterization. *Quart. J. Roy. Meteor. Soc.,* **99,** 178–196.

Blyth, A., 1993: Entrainment in cumulus clouds. *J. Appl. Meteor.,* **32,** 626–641.

Bony, S., and K. A. Emanuel, 2001: A parameterization of the cloudiness associated with cumulus convection; evaluation using TOGA COARE data. *J. Atmos. Sci.,* **58,** 3158–3183.

——, and Coauthors, 2006: How well do we understand and evaluate climate change feedback processes? *J. Climate,* **19,** 3445–3482.

Bretherton, C. S., and P. K. Smolarkiewicz, 1989: Gravity waves, compensating subsidence and detrainment around cumulus clouds. *J. Atmos. Sci.,* **46,** 740–759.

Brown, A., and Coauthors, 2002: Large-eddy simulation of the diurnal cycle of shallow cumulus convection over land. *Quart. J. Roy. Meteor. Soc.,* **128,** 1075–1093.

Chatfield, R. B., and R. A. Brost, 1987: A two-stream model of the vertical transport of trace species in the convective boundary layer. *J. Geophys. Res.,* **92,** 13 263–13 276.

Coindreau, O., F. Hourdin, M. Haeffelin, A. Mathieu, and C. Rio, 2007: Assessment of physical parameterizations using a global climate model with stretchable grid and nudging. *Mon. Wea. Rev.,* **135,** 1474–1489.

Deardorff, J. W., 1972: Theoretical expression for the countergradient vertical heat flux. *J. Geophys. Res.,* **77,** 5900–5904.

Dufresne, J.-L., J. Quaas, O. Boucher, S. Denvil, and L. Fairhead, 2005: Contrasts in the effects on climate of anthropogenic sulfate aerosols between the 20th and the 21st century. *Geophys. Res. Lett.,* **32,** L21703, doi:10.1029/2005GL023619.

Emanuel, K. A., 1991: A scheme for representing cumulus convection in large-scale models. *J. Atmos. Sci.,* **48,** 2313–2335.

——, 1993: A cumulus representation based on the episodic mixing model: The importance of mixing and microphysics in predicting humidity. *The Representation of Cumulus Convection in Numerical Models of the Atmosphere, Meteor. Monogr.,* No. 46, Amer. Meteor. Soc., 185–192.

Fouquart, Y., and B. Bonnel, 1980: Computations of solar heating of the Earth's atmosphere: A new parametrization. *Contrib. Atmos. Phys.,* **53,** 35–62.

Grandpeix, J.-Y., V. Phillips, and R. Tailleux, 2004: Improved mixing representation in Emanuel's convection scheme. *Quart. J. Roy. Meteor. Soc.,* **130,** 3207–3222.

Guichard, F., and Coauthors, 2004: Modelling the diurnal cycle of deep precipitating convection over land with cloud-resolving models and single-column models. *Quart. J. Roy. Meteor. Soc.,* **130,** 3139–3172.

Haeffelin, M., and Coauthors, 2005: SIRTA, a ground-based atmospheric observatory for cloud and aerosol research. *Ann. Geophys.,* **23,** 253–275.

Holtslag, A. A. M., and B. A. Boville, 1993: Local versus nonlocal boundary-layer diffusion in a global climate model. *J. Climate,* **6,** 1825–1842.

Hourdin, F., F. Couvreux, and L. Menut, 2002: Parameterization of the dry convective boundary layer based on a mass flux representation of thermals. *J. Atmos. Sci.,* **59,** 1105–1123.

——, and Coauthors, 2006: The LMDZ4 general circulation model: Climate performance and sensitivity to parametrized physics with emphasis on tropical convection. *Climate Dyn.,* **27,** 787–813.

Lappen, C.-L., and D. Randall, 2001a: Toward a unified parameterization of the boundary layer and moist convection. Part I: A new type of mass-flux model. *J. Atmos. Sci.,* **58,** 2021–2036.

——, and ——, 2001b: Toward a unified parameterization of the boundary layer and moist convection. Part II: Lateral mass exchanges and subplume-scale fluxes. *J. Atmos. Sci.,* **58,** 2037–2051.

——, and ——, 2001c: Toward a unified parameterization of the boundary layer and moist convection. Part III: Simulations of clear and cloudy convection. *J. Atmos. Sci.,* **58,** 2052–2072.

Lenderink, G., and Coauthors, 2004: The diurnal cycle of shallow cumulus clouds over land: A single column model intercomparison study. *Quart. J. Roy. Meteor. Soc.,* **130,** 3339–3364.

Lilly, D., 1968: Models of cloud-topped mixed layers under a strong inversion. *Quart. J. Roy. Meteor. Soc.,* **94,** 292–309.

Mellor, G. L., and T. Yamada, 1974: A hierarchy of turbulence closure models for planetary boundary layers. *J. Atmos. Sci.,* **31,** 1791–1806.

Moeng, C.-H., and P. P. Sullivan, 1994: A comparison of shear- and buoyancy-driven planetary boundary layer flows. *J. Atmos. Sci.,* **51,** 999–1022.

Morcrette, J. J., L. Smith, and Y. Fouquart, 1986: Pressure and temperature dependence of the absorption in longwave radiation parameterizations. *Contrib. Atmos. Phys.,* **59,** 455–469.

Neggers, R. A. J., A. P. Siebesma, and H. J. J. Jonker, 2002: A multiparcel model for shallow cumulus convection. *J. Atmos. Sci.,* **59,** 1655–1668.

Pleim, J. E., and J. S. Chang, 1992: A non-local closure model for vertical mixing in the convective boundary layer. *Atmos. Environ.,* **26A,** 965–981.

Randall, D. A., Q. Shao, and C.-H. Moeng, 1992: A second-order bulk boundary-layer model. *J. Atmos. Sci.,* **49,** 1903–1923.

Raymond, D. J., and A. M. Blyth, 1986: A stochastic model for nonprecipitating cumulus clouds. *J. Atmos. Sci.,* **43,** 2708–2718.

Siebesma, A. P., and J. W. M. Cuijpers, 1995: Evaluation of parametric assumptions for shallow cumulus convection. *J. Atmos. Sci.,* **52,** 650–666.

——, and A. A. M. Holtslag, 1996: Model impacts of entrainment and detrainment rates in shallow cumulus convection. *J. Atmos. Sci.,* **53,** 2354–2364.

——, and Coauthors, 2003: A large eddy simulation intercomparison study of shallow cumulus convection. *J. Atmos. Sci.,* **60,** 1201–1219.

——, P. M. M. Soares, and J. Teixeira, 2007: A combined eddy-diffusivity mass-flux approach for the convective boundary layer. *J. Atmos. Sci.,* **64,** 1230–1248.

Soares, P. M. M., P. M. A. Miranda, A. P. Siebesma, and J. Teixeira, 2004: An eddy-diffusivity/mass-flux parameterization for dry and shallow cumulus convection. *Quart. J. Roy. Meteor. Soc.,* **130,** 3365–3383.

Stevens, B., 2007: On the growth of layers of nonprecipitating cumulus convection. *J. Atmos. Sci.,* **64,** 2916–2931.

Stull, R. B., 1984: Transilient turbulence theory. Part I: The concept of eddy-mixing across finite distances. *J. Atmos. Sci.,* **41,** 3351–3367.

Suarez, M., A. Arakawa, and D. Randall, 1983: The parameterization of the planetary boundary layer in the UCLA general circulation model: Formulation and results. *Mon. Wea. Rev.,* **111,** 2224–2243.

Tiedtke, M., 1989: A comprehensive mass flux scheme for cumulus parameterization in large-scale models. *Mon. Wea. Rev.,* **117,** 1779–1800.

Troen, I., and L. Mahrt, 1986: A simple model of the atmospheric boundary layer: Sensitivity to surface evaporation. *Bound.-Layer Meteor.,* **37,** 129–148.

Wang, S., and B. A. Albrecht, 1990: A mean-gradient model of the dry convective boundary layer. *J. Atmos. Sci.,* **47,** 126–138.

Yamada, T., 1983: Simulations of nocturnal drainage flows by a $q^2l$ turbulence closure model. *J. Atmos. Sci.,* **40,** 91–106.

Yanai, M., S. Esbensen, and J.-H. Chu, 1973: Determination of bulk properties of tropical cloud clusters from large-scale heat and moisture budgets. *J. Atmos. Sci.,* **30,** 611–627.

Zhang, M. H., and Coauthors, 2005: Comparing clouds and their seasonal variations in 10 atmospheric general circulation models with satellite measurements. *J. Geophys. Res.,* **110,** D15S02, doi:10.1029/2004JD005021.

Zhao, M., and P. H. Austin, 2003: Episodic mixing and buoyancy-sorting representations of shallow convection: A diagnostic study. *J. Atmos. Sci.,* **60,** 892–912.

——, and ——, 2005a: Life cycle of numerically simulated shallow cumulus clouds. Part I: Transport. *J. Atmos. Sci.,* **62,** 1269–1290.

——, and ——, 2005b: Life cycle of numerically simulated shallow cumulus clouds. Part II: Mixing dynamics. *J. Atmos. Sci.,* **62,** 1291–1310.